Additive manufacturing of multiscale NiFeMn multi-principal element alloys with tailored composition

Shahryar Mooraj[1,4]**, Jintao Fu**[2,4]**, Shuai Feng**[1]**, Alexander K Ng**[2]**, Eric B Duoss**[3]**, Sarah E Baker**[3]**, Cheng Zhu**[3]**, Eric Detsi**[2,*]** and Wen Chen**[1,*]

[1] Department of Mechanical and Industrial Engineering, University of Massachusetts, Amherst, MA 01003-2210, United States of America
[2] Department of Materials Science & Engineering, University of Pennsylvania, Philadelphia, PA 19104-6272, United States of America
[3] Lawrence Livermore National Laboratory, 7000 East Avenue, Livermore, CA 94550, United States of America

E-mail: detsi@seas.upenn.edu and wenchen@umass.edu

CrossMark

Abstract

Nanostructured multi-principal element alloys (MPEAs) have been explored as next-generation engineering materials due to unique mechanical and functional properties which have significant advantages over traditional dilute alloys. However, the practical applications of nanostructured MPEAs are still limited due to the lack of scalable processing approaches to prepare a large quantity of nanostructured MPEAs, as well as lack of an efficient pathway for high-throughput discovery of better functional nanostructured MPEAs within their vast compositional space. Here we tackle these challenges by presenting an integrated approach by combining direct-ink-writing-based additive manufacturing, solid-state sintering, and chemical dealloying to manufacture hierarchically porous MPEAs. The hierarchical structure is comprised of macro- and micro-scale pores introduced via extrusion printing and polymer decomposition during sintering, as well as nanoscale pores formed via chemical dealloying. The macro- and micro-scale pores allow efficient dealloying of a large mass of material as the diffusion length that the corroding medium must penetrate remains at the scale of the ligaments formed after sintering ($\sim$10 μm), despite the large volume of the 3D-printed samples. In addition, this integrated approach enables versatile control of the alloy composition via precisely tuning the ratio of elemental powders in the starting ink, thus offering a pathway for high-throughput discovery of novel functional MPEAs. As a case study, multiscale macro/micro/nanoporous NiFeMn MPEAs with three different compositions were investigated as catalysts to reduce the overpotential of oxygen evolution reaction (OER), where NiFeMn-based electrocatalysts display composition-dependent performance such that the overpotential measured at a current of 0.5 A g^{-1} for OER increases in the order of Ni$_{58}$Fe$_{29}$Mn$_{13}$ $\leqslant$ Ni$_{64}$Fe$_{26}$Mn$_{10}$ < Ni$_{76}$Fe$_{18}$Mn$_6$. This introduced manufacturing process offers new opportunities for scalable fabrication and rapid screening of nanostructured multi-component complex alloys.

[4] These authors contributed equally.
[*] Authors to whom any correspondence should be addressed.

1. Introduction

In recent years, multi-principal element alloys (MPEAs) with earth-abundant elements are gaining an increasing attention in the fields of corrosion resistance, (electro)catalysis, medical application, among others [1–3]. These alloys also show impressive properties of high ductility [4], interesting deformation behavior [5] and superior fatigue resistance [6]. MPEAs are a class of metal alloys based on random mixing of multi-principal elements that exhibit improved mechanical and functional properties over traditional dilute alloys [7–14], which often have only one or two major elements doped with other minor elements [15–17]. Nanostructuring of MPEAs in the form of nanoparticles, nanoporous materials, and nanowires [18, 19] can provide additional unique advantages including a large specific surface area which improves reaction rate in (electro)catalysis [20, 21]. Despite these advantages, nanostructured MPEAs suffer from two distinct challenges which limit their practical applications. First, most synthesis methods for nanostructured materials are limited to production of thin films or ribbons that are difficult to scale up and expensive to implement at commercial levels [22–25]. For instance, the typical production of nanoporous metals is based on chemical dealloying [26–28], where the dealloying time becomes impractically long for bulk materials compared to thin films. An overlong dealloying time results in a more coarse porous structure, eroding the nanostructure and thus reducing the chemically active surface area [29, 30]. Therefore, dealloying a large mass of material is not practical by existing technologies. The second challenge arises due to the vast compositional space encompassed by MPEAs [31–36]. The multi-principal element nature of MPEAs offers an enormous material design space to explore new compositions at the central region of the phase diagram [37, 38]. While this new design paradigm provides a unique opportunity to discover novel materials, it also presents a significant challenge as the number of candidate compositions is too large to study in a reasonable amount of time. Thus, researchers need to explore new workflows to expedite fabrication and property screening of MPEAs with different compositions [39]. To date, many methods to produce MPEAs for exploration of functional properties involve using complex precursor materials such as oxides or using traditional synthesis methods such as arc melting to produce specific alloys, which require lengthy processing times for preparing and studying each individual composition [7, 40, 41].

This work presents a novel integrated approach towards preparation of nanostructured MPEAs by combining material extrusion-based 3D printing (or direct ink writing, DIW), solid-state sintering, and chemical dealloying to achieve a series of hierarchically porous MPEAs. DIW is an additive manufacturing method which enables 3D printing of architected structures where the size of macroscale channels/pores can be digitally engineered [42, 43]. After printing, heat treatment of the printed MPEA structures enables removal of polymer binder and solvents as well as thermal sintering of the metal particles, during which the dimension and concentration of microscale porosity ($\sim$10 μm) can be engineered via controlling the degree of sintering or densification. Lastly, nanoscale porosity is introduced via chemical dealloying of the sintered MPEA structure, during which the excess sacrificial element is selectively dissolved into the corroding medium. The presence of macro/micro-scale hierarchical structure after DIW and sintering allows chemical dealloying to produce nanoscale pores in a large mass of 3D MPEA architectures within a short dealloying time, owing to the reduced diffusion length of corroding medium compared to their dense counterparts. In addition, our integrated approach is capable of controlling the composition by using elemental powders with different ratios in the starting ink, thus enabling the efficient search for better functional MPEAs in the vast compositional space. As an illustration of this approach, we prepared multiscale macro/micro/nanoporous NiFeMn MPEAs with three different compositions and tested them as oxygen evolution reaction (OER) electrocatalysts. This system utilizes relatively cheap elements compared to most OER catalysts which rely on expensive precious metals [44]. We show that OER performance of our catalysts was composition-dependent, such that the overpotential measured at a current of 0.5 A g^{-1} for OER increases in the order of $\mathrm{Ni_{58}Fe_{29}Mn_{13}} \leqslant \mathrm{Ni_{64}Fe_{26}Mn_{10}} < \mathrm{Ni_{76}Fe_{18}Mn_6}$. This work presents a new avenue for high-throughput discovery as well as highly scalable production of nanostructure MPEA functional materials.

2. Materials and methods

2.1. DIW of elemental powders

DIW is a low-cost method of additive manufacturing that allows for 3D printing of materials into a vast array of geometries with high resolution. When utilizing DIW, samples are constructed in a layer by layer fashion via deposition of filaments made of particulate suspensions [45]. These suspensions typically contain micron-sized particles dispersed homogeneously within a solution of organic solvents and a dissolved polymer binder. An element of this method involved formulating inks with suitable shear-thinning rheological properties. These properties allow the ink to flow smoothly through a narrow-tipped nozzle (200 μm) when a shear force is applied which guarantees the formation of continuous filaments maintained by steady pressure or displacement rate. Then, once these filaments exit the nozzle these inks can retain their shape and dry rapidly due to the evaporation of volatile solvents. The rheology of the ink is adjusted by tuning the particle to binder

ratio. In this study, we expand upon our recent results relating to 3D hierarchically nanoporous Cu [46], the NiFeMn ternary MPEA inks were formulated by combining separate powders of Ni, Fe, and Mn (APS 10 μm, >99.6%, Alfa Aesar) with a PMMA-PnBA bi-block copolymer which acted as a binder and organic solvents of 2-butoxyethanol and tetrahydrofuran (THF). The binder polymer was dissolved in the THF and 2-butoxyethanol mixture, and then the metal powders were added to produce the initial ink. To demonstrate the versatility of compositional design within DIW-based additive manufacturing technique, we synthesized three ternary MPEA inks prepared with different overall compositions of $Ni_{14}Fe_{18}Mn_{68}$ (at. %), $Ni_{12}Fe_{15}Mn_{73}$ (at. %), and $Ni_9Fe_{11}Mn_{80}$ (at. %). The ink's volumetric ratio of metallic powder to binding polymer was maintained at 65:35 for all the inks presented in this work. The inks exhibit the expected shear-thinning characteristic with a suitable range of viscosity of 10^2–10^5 Pa · s that enables the DIW process (figure 1). For 3D structure fabrication, the ink is loaded into a syringe-barrel (Nordson EFD) and deposited onto a planar alumina substrate by pressurizing the printhead with compressed air to direct the ink through a tapered nozzle with a 200 μm tip diameter under digital control. As the ink was extruded through the nozzle, the THF rapidly evaporated, leaving behind solid filaments after deposition. Woodpile lattice structures measuring 5 mm × 5 mm × 3 mm were fabricated with a layer height of 0.15 mm and 0.5 mm hatch spacing between tracks at a scan rate of 10 mm s^{-1}. We also produced larger samples for visualization (figure 2). Samples in the as-printed state consisted of individual Fe, Mn, and Ni particles held together thanks to the block copolymer.

2.2. Thermal sintering of metal particles

To form chemically homogeneous NiFeMn ternary MPEA architectures, a heat treatment protocol utilizing multiple heating steps was executed in an OTF-1700X furnace (MTI Corporation) to a maximum temperature of 1100 °C. The process began with heating the samples to 100 °C for 1 h to volatilize residual THF followed by heating to 220 °C for 1 h to remove the 2-Butoxyethanol solvent. The samples were then heated to 420 °C to decompose the polymer binder, and finally sintered at 1100 °C for 15 h to consolidate and alloy the metal powders. A constant heating rate of 5 °C min^{-1} was used between each processing step and was carried out under an ultrahigh-purity Ar atmosphere to avoid oxidation during sintering. Samples were finally furnace-cooled to room temperature. We are able to calculate the expected diffusion length for complete sintering of each element by using Fick's Law [47]. The diffusion length is given by the equation: $L = (2D \cdot t)^{1/2}$, where D is the diffusion coefficient and t is the sintering time. While diffusion within a ternary MPEA system can be difficult to estimate without extensive simulation, the diffusion coefficient for the binary systems of Mn–Ni, Mn–Fe, and Ni–Fe has been previously reported. We can use these results to estimate the diffusion lengths of each pair of elements within the sintered ternary MPEA samples. Specifically, for Mn-Ni, the diffusion constant was reported by Yokota *et al* as

2×10^{-13} m^{2}s^{-1} at 1050 °C [48]. Based on Hedge *et al* the inter-diffusivity of Mn–Fe can be estimated as 2.5×10^{-13} m^{2}s^{-1} [49]. Finally, Million *et al* reported the diffusion constant for Ni–Fe as approximately 1×10^{-14} m^2 s^{-1} at 1100 °C [50]. Using these values for the diffusion constants and considering the sintering time (15 h) in this study, we can estimate the diffusion lengths in the sintered samples for the Mn–Ni, Mn–Fe and Ni–Fe binary systems as 147 μm, 164 μm, and 33 μm, respectively. These calculated values are at least three times larger than the initial particle size of the elemental powders (approximately 10 μm) used for starting ink preparation. Therefore, we expect to achieve a homogeneous alloy after sintering.

2.3. Chemical dealloying

Nanoporous materials can be synthesized by chemical dealloying, which involves selectively removing the most reactive elements of a parent alloy using an appropriate corroding medium, leading to the formation of nanoscale voids and nanoscale struts known as ligaments. In the case of Ni-Fe-Mn system, the corroding medium used for chemical dealloying was a 1 M solution of ammonium sulfate, and the dealloying time was 4 d. The solution was refreshed every 24 h to maintain a high dealloying rate. During this process, Mn and Fe, which are both more active than Ni, were gradually removed from the alloys. Since Mn dissolves more readily than Fe in ammonium sulfate, its decrease in atomic content is more prominent than the decrease in Fe content. After dealloying, we washed the samples using deionized water and vacuum-dried them at room temperature.

2.4. Material characterization

A JEOL 7500 F scanning electron microscopy (SEM) which had an energy dispersive spectroscopy (EDS) sensor was used to analyze the microstructure and elemental composition of the as-sintered and dealloyed samples. The bulk composition of these materials is further investigated using inductively coupled plasma optical emission spectroscopy (ICP-OES). X-ray diffraction (XRD) spectra were measured via a Rigaku Miniflex powder diffractometer (Cu x-ray source, operated at 40 kV/15 mA) with 0.02° step size and a 3° min^{-1} scanning rate to analyze phase constitutions in the sintered and dealloyed samples. A ternary phase diagram of NiFeMn was also generated using FactSage to help understand the expected phase transformation during sintering. Small-angle x-ray scattering (SAXS) was performed at the Dual Source and Environmental x-ray Scattering facility at University of Pennsylvania with detection limited to sizes between 1 Å and 570 nm in order to probe the nanoscale pores as well as obtain an estimation of the average nanopore size [51–53].

2.5. Electrocatalytic OER

To investigate the electrocatalytic OER performance of multiscale macro/micro/nanoporous NiFeMn ternary MPEAs

as a case study, a slurry-type electrode was prepared by breaking up the 3D printed structure into powder form and mixing the micro/nanoporous NiFeMn ternary MPEA powders with conductive carbon powder and a polyvinylidene fluoride binder (mass ratio 7:2:1), the mixture was dried under vacuum at room temperature. The samples were crushed into a slurry to improve the diffusion kinetics of reactant/products during electrochemical testing as diffusion through the printed filaments is sluggish. Cyclic voltammetry (CV) was carried out in 1 M NaOH solution, with the slurry NiFeMn ternary MPEA as the working electrode, a Pt wire as the counter electrode, and Hg/HgO (1 M NaOH filling electrolyte) as the reference electrode. The scan rate was 1 mV s^{-1}. A galvanostatic OER stability test was carried out under the same condition mentioned above. A constant stirring of 300 rpm was also applied during the stability test to facilitate the mass transport of electrolyte species. All of the measured potentials were converted to a scale relative to a reversible hydrogen electrode (RHE) utilizing the following equation:

$$E\,(\text{versus RHE}) = E\,(\text{versus Hg/HgO}) + 0.140\ \text{V} + 0.0591\ \text{V} * \text{pH}.$$
(1)

3. Results and discussion

3.1. Synthesis of multiscale NiFeMn structure

The viscosity of the NiFeMn MPEA inks depends strongly on the volume fractions of polymer binder and solvents used. Adding the solvents ensured the homogeneous mixing and formulation of NiFeMn inks with gel-like behavior that exhibits suitable printability. Figure 1 presents the rheological properties of a typical NiFeMn MPEA ink used for printing lattice geometries in this work. Figure 1(a) shows that the apparent viscosity of the ink falls as the applied shear rate increases. This result shows that the ink exhibits shear-thinning properties, which allows the ink to flow continuously when shear stress is applied while retaining the filamentary shape after exiting from the nozzle with release of the shear stress. Figure 1(b) shows the elastic (G') and viscous (G'') moduli of the ink plotted versus the applied shear stress. The elastic modulus is also known as the storage modulus, which represents the capacity of a fluid to store elastic energy. In contrast, the viscous modulus illustrates the ink's capacity to dissipate energy during deformation, which describes the viscous response of the material. Once the shear stress acting on the ink reaches above 100 Pa, the elastic modulus decreases such that it drops beneath the loss modulus, and the ink exhibits liquid-like properties and can readily flow out of the nozzle. Once the ink leaves the nozzle tip, it stops experiencing any shear stress, and thus the elastic and viscous moduli are restored which makes the ink act like a solid. Additionally, the rapid evaporation of the volatile organic solvents allows the ink to dry rapidly and ensures the polymer binder to hold the metal powders together. These properties ensure that the extruded filaments can retain their shape after exiting the nozzle.

Additionally manufactured hierarchical NiFeMn MPEA samples were synthesized by DIW, the samples were dried overnight and subsequently subjected to solid-state thermal sintering, and dealloying, as shown in figure 2. The architected ternary MPEAs exhibit a hierarchical structure that spans several orders of magnitude—from centimeters to nanometers. The macro- and meso-scale pores are designed by a robot-controlled DIW process and therefore, these large pores exhibit a highly controlled shape and spatial distribution. These features are printed with a high resolution that is defined by the printed filament diameter. This filament diameter is about 150–250 μm, as shown in figures 2(h)–(j). It is possible to further refine this feature size by reducing the ink particle size (e.g. using nanoparticle instead of micron-sized particles), shrinking the nozzle size (200 μm for this study) and tuning the ink rheology. Within this hierarchical structure, micrometer-sized pores ranging from ∼1–10 μm, result from the volatilization of the solvent and polymer binder decomposition (figures 2(k) and (l)). The microscale pore distrbution can be adjusted by varying the solvents to polymer binder volumetric ratios as long as the ink maintains a viscosity and a shear-thinning characteristic that is suitable to retain the ink's printability [54]. The macro-, meso-, and micro-scale pores, measured from multiple SEM images, enhance mass transport throughout the ternary MPEA catalysts, accelerating reaction kinetics [55]. Thermal solid-state sintering converts the constituent Mn, Ni, and Fe micro-particles into a homogeneous NiFeMn alloy (figures 2(k) and (l)), while the later dealloying process generates nanoscale pores of around 10 nm (figures 2(m) and (n)). The nanopores in this work show a smooth and bicontinuous morphology throughout the entire 3D-printed structure. The morphology of these nanoscale pores is normally governed by the dealloying conditions, including the type of dealloying media and the duration of the process [56]. SAXS is used to quantitatively measure the average pore diameter, to be discussed in section 3.2.

Thus far, chemical dealloying is often carried out by immersing a material in the form of thin film or ribbon inside a corrosive medium to selectively leach the most reactive components of an alloy [57]. Thin films or ribbons are used to minimize the dealloying time since the medium must penetrate the entire sample to form a complete 3D nanostructure. As a result, only a small amount of dealloyed nanostructured/nanoporous material can be obtained [58]. Traditionally manufactured bulk samples can provide larger amounts of material, however, these samples require much longer dealloying time which leads to coarsening of the nanostructures, resulting in decreased surface area [59–62]. Thus, a facile design of the bulk sample is necessary in order to enhance the dealloying efficiency. The 3D-printed multiscale NiFeMn MPEA structures shown in this study allow accelerated dealloying efficiency for scalable manufacturing of nanoporous materials as the diffusion length that the corroding medium must penetrate remains at the scale of the ligaments formed after polymer burnout and sintering (∼10 μm, figure 2(k)). This diffusion length is comparable to many thin films or ribbons and hence allows a large sample mass of the printed architecture
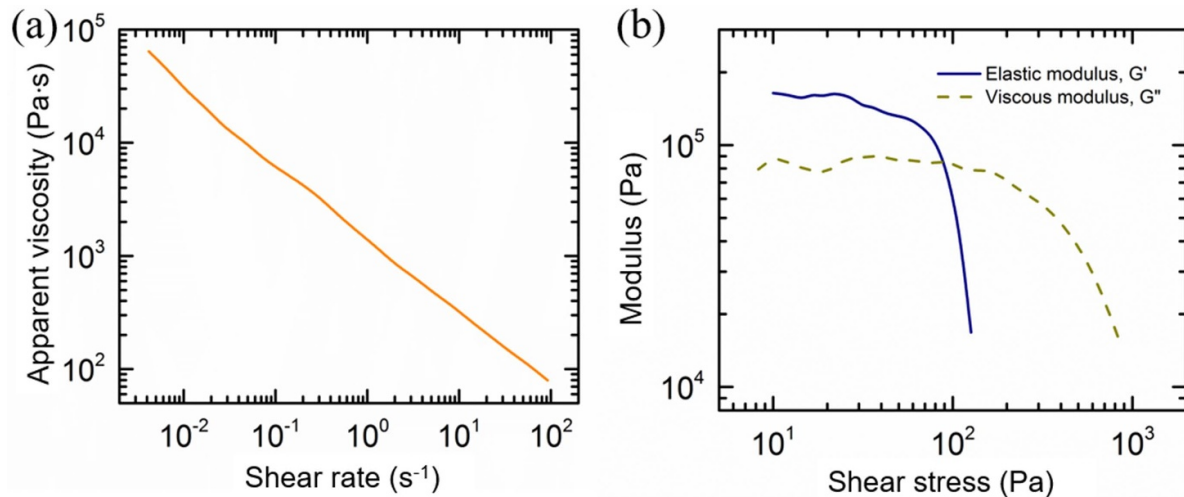
Figure 1. Log–log plots of (a) measured viscosity vs. the shear rate, (b) elastic (G'), and viscous (G'') modulus plotted against shear stress of a typical NiFeMn ink.

to be dealloyed in a geometrically compact form while keeping a similar length scale for diffusion. Thus, the DIW process illustrated here offers a unique opportunity to rapidly scale the production of nanoporous materials while maintaining a practically short dealloying time for the retention of the desired nanoporous structure.

To properly dealloy the sintered NiFeMn MPEA specimens, the constituent metal particles must be fully alloyed to ensure that the more reactive elements (Mn and Fe) form a percolating network throughout the structure. This network enables the corroding medium to find a continuous pathway to travel through the entire structure [63]. If the alloying process is incomplete due to insufficient sintering temperature or time, the Mn and Fe atoms cannot fully disperse through the structure and consequently areas with lower concentrations of Mn and Fe will not be included in the percolation network, leading to reduced chemically active specific area of the nanoporous network. It is well known that the kinetics of atomic diffusion depend strongly on the heat treatment temperature [64]. Thus, the sintering temperature must remain high enough that the diffusivities of the Mn, Ni and Fe atoms are above a threshold where alloying and atomic dispersion can occur throughout the 3D-printed architecture while below the melting temperature of the alloy compositions to ensure the 3D-printed structure remains intact after sintering. Figure 3 shows the ternary phase diagram of NiFeMn at 1100 °C and at 25 °C generated via FactSage. It is seen that a single-phase face-centered cubic (FCC) solid solution is expected at 1100 °C for the considered ternary MPEAs. At 25 °C, we note that a triple phase structure is predicted including a body-centered cubic (BCC) solid solution, a complex BCC solid solution and a Mn_3Ni intermetallic phase. It should be noted that these phase diagrams indicate the expected phases at equilibrium, meaning the sintering needs be held long enough at 1100 °C to ensure the complete formation of the FCC solid solution. Once the sintering process is completed, the samples are furnace-cooled, but no secondary phases were observed to form in this work

(figure 4). The lack of secondary phase is likely due to the slow diffusion kinetics of the atoms at lower temperatures which prevents the decomposition of the metastable FCC phase at low temperatures. Previously, many MPEAs have been shown to form metastable solid solutions with high thermal stability owing to the sluggish diffusion within such systems [65, 66].

The phase constituents of the three considered ternary MPEAs were further confirmed by XRD. Figure 4 illustrates the XRD profiles of all three NiFeMn MPEAs before and after dealloying. These results indicate that a single-phase FCC solid solution [67] is indeed present after sintering with no secondary phases or pure elemental phases, implying that the elemental particles were fully alloyed and that the samples were suitable for chemical dealloying. Figure 4 also shows a significant broadening of the peaks after dealloying which is due to the nanoscale features within the structure [68], but the FCC crystal structure is still maintained. As previously discussed, a common trait among many MPEAs is the sluggish diffusion kinetics that help suppress the precipitation of thermodynamically more stable (or energetically more favorable) phases at lower temperatures, and thus such systems often appear as metastable solid solutions at room temperature [66]. It is therefore unsurprising that the FCC structure remains stable during dealloying as the procedure was carried out at room temperature, which would prevent fast atomic rearrangement that is necessary to form new phases.

3.2. Composition investigation and morphology characterization

The inherent multi-principal element nature of MPEA systems endows an enormous compositional space for alloy design. One important goal of this work is to illustrate the flexibility offered by the DIW to accelerate the pace of alloy exploration. By adjusting the composition of the ink, we can readily achieve MPEAs with different compositions after sintering of the ink. Furthermore, the different sintered MPEA
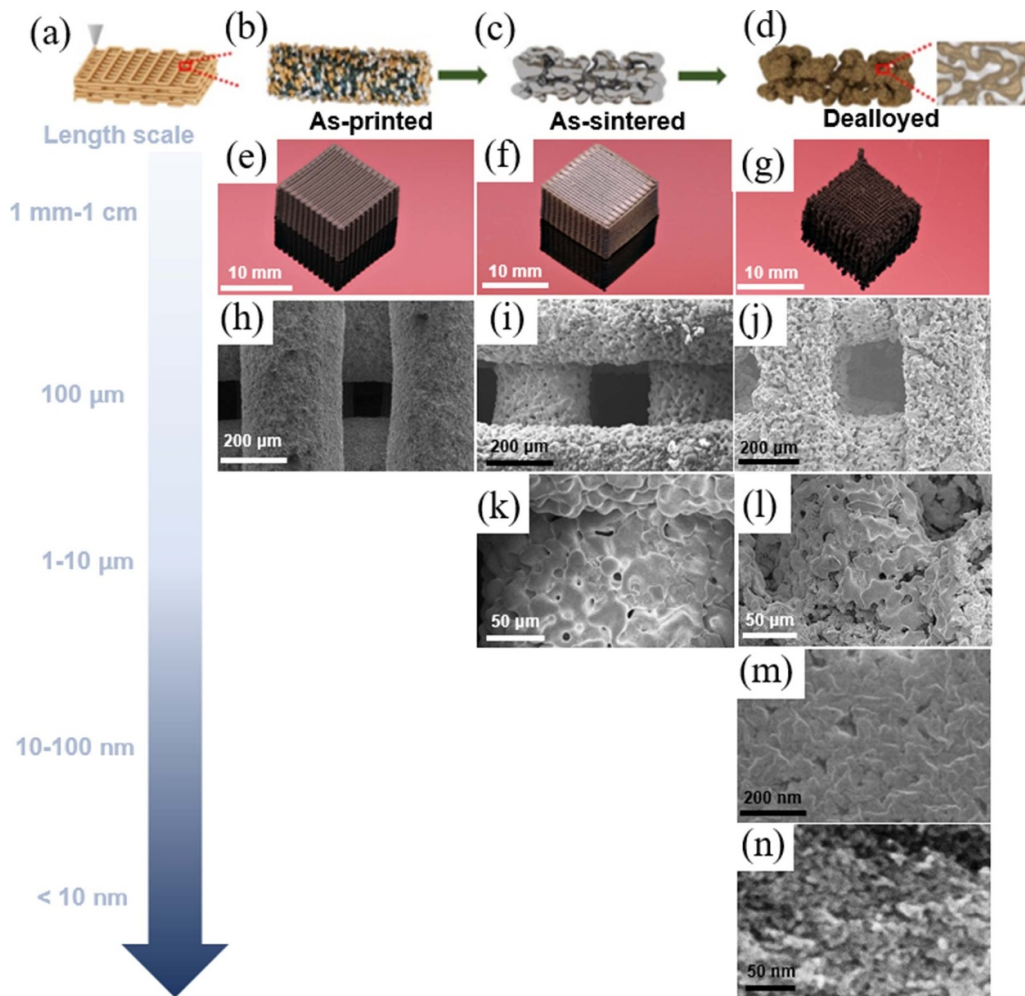
Figure 2. Development of features at various length scales in the 3D-printed hierarchically porous NiFeMn MPEAs during processing of these samples. (a)–(b) Schematic representation of direct writing of inks made from mixed particles of Mn, Ni, and Fe elemental powders, along with a polymer binder as well as organic solvents. DIW precisely controls the macroscale and mesoscale porosity. (c) Thermal solid-state sintering results in the alloying of Ni, Fe, and Mn powders, the volatilization of organic solvents, and the decomposition of the polymer binder to produce microscale porosity. (d) The dealloying step dissolves Mn and Fe components in the alloy to create the nanoscale porosity. Optical images depict multilayer woodpile-like architectures at mm-cm scales in various states: as-printed (e), sintered (f), and dealloyed (g). SEM images reveal the structural evolution at different stages—printing, thermal sintering, and dealloying—across multiple length scales: 100 μm scale (h)–(j), 10 μm scale (k)–(l), and 10–100 nm scale (m)–(n).

compositions lead to different compositions after dealloying, as seen in table 1, which presents the sintered and dealloyed NiFeMn MPEA compositions measured via both EDS and ICP. It should be noted that the minor discrepancy in alloy composition of the sintered and as-printed alloys may arise from the slight losses of some elements due to vaporization during sintering. Both measurement methods are in good agreement. The EDS results were averaged from 3 different regions in each sample, while the ICP results indicate the overall composition of each sample. Notably, a larger initial Mn content in the sintered NiFeMn MPEAs tends to result in a lower Mn content after dealloying. This is because a higher Mn content leads to higher exposure of Mn atoms to the corroding medium. Fe reacts much more slowly with the corroding medium than Mn does, and Ni does not react at all. Since more Mn atoms are within the structure, they form a more

interconnected network that provides favorable paths for the penetration and transport of the corroding medium. Therefore, when Mn content is higher, the rate of dealloying is significantly increased. The faster dealloying induces a lower residual Mn content after the same dealloying time.

SAXS is a reciprocal space technique which offers representative insights into nanoscale feature sizes [69, 70], and was performed to confirm the nanoscale features after dealloying, as shown in figure 5. During SAXS, the nanoscale features in the material scatter the incident x-ray beam and are represented by a peak in the scattering plot. Generally, nanoporous structures yield a broad peak, because there is a distribution of pore sizes and ligament sizes throughout this material, with the most prominent structure size being represented by *q*-value associated with the maximum intensity of the peak. The SAXS pattern of the as-sintered NiFeMn
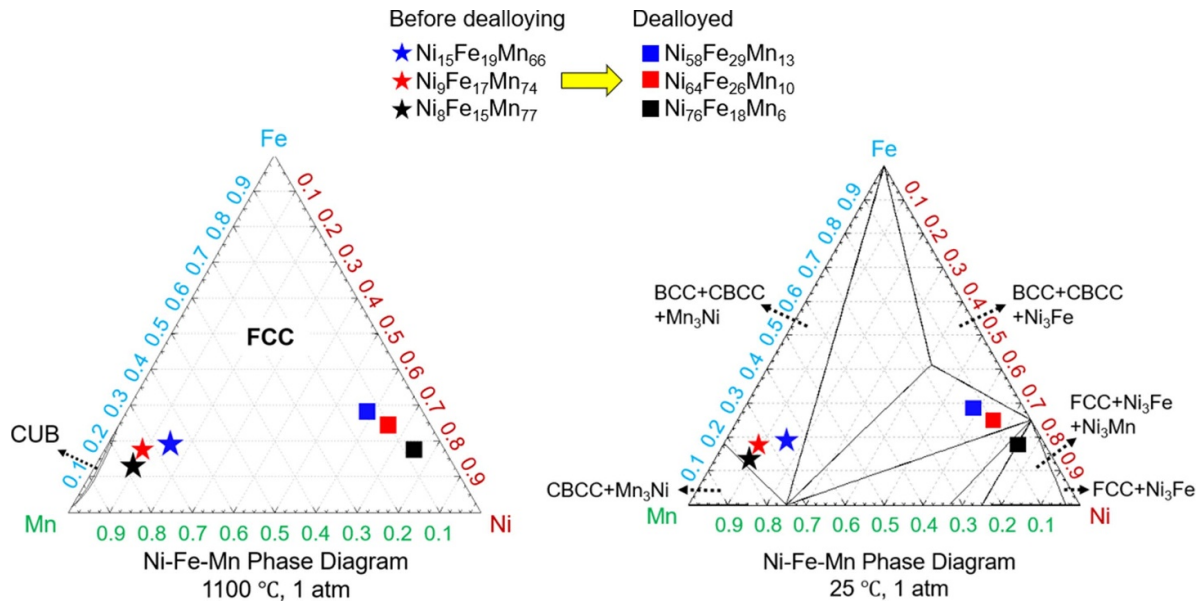
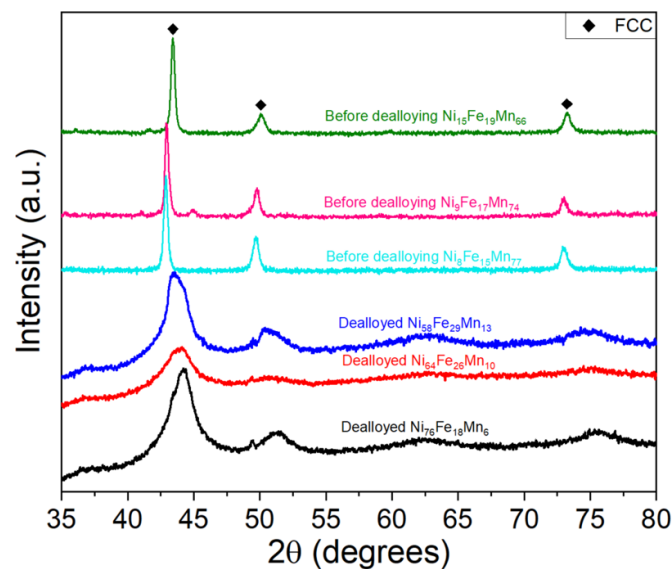**Figure 3.** Ternary phase diagrams of Ni–Fe–Mn at 1100 °C and 25 °C generated via FactSage.

Figure 4. XRD patterns of as-sintered $Ni_{15}Fe_{19}Mn_{66}$, $Ni_8Fe_{15}Mn_{77}$, and $Ni_9Fe_{17}Mn_{74}$ MPEAs and the corresponding dealloyed $Ni_{58}Fe_{29}Mn_{13}$, $Ni_{64}Fe_{26}Mn_{10}$, and $Ni_{76}Fe_{18}Mn_6$ MPEAs. The FCC phase is identified based on previously reported XRD patterns of the NiFeMn system [67].

MPEAs before dealloying clearly shows a straight line, as seen in the representative sample of $Ni_8Fe_{15}Mn_{77}$. The other two as-sintered NiFeMn MPEAs exhibit similar SAXS patterns and are not shown. This straight-line SAXS patten indicates an there is no repeating nanostructure. In contrast, the SAXS spectra of the three considered dealloyed samples show a peak at $q \approx 0.075$ Å^{-1}, 0.065 Å^{-1}, 0.055 Å^{-1} for $Ni_{64}Fe_{26}Mn_{10}$ (red curve), $Ni_{58}Fe_{29}Mn_{13}$ (blue curve), and $Ni_{76}Fe_{18}Mn_6$ (black curve), respectively. The position of this peak in the q-space can be modified to a characteristic size (d)

in real space, namely the ligament-to-ligament distance, utilizing the equation [51–53]: $d = 1.23 \times (2\pi/q)$. The $Ni_{76}Fe_{18}Mn_6$ peak thus yields an average ligament-to-ligament distance of $d \approx 14$ nm. The mean diameter of the ligaments and pores are around half of the ligament-to-ligament distance, specifically it measured to be 7 nm. Figure 6 shows SEM and TEM images of the dealloyed $Ni_{76}Fe_{18}Mn_6$. Here, the nanoporous structure of the sample can be clearly resolved, and the average pore diameter is approximately 5–10 nm, which agrees well with the estimated value based on the SAXS data.

Table 1. Average chemical compositions of the sintered and dealloyed NiFeMn MPEA samples.

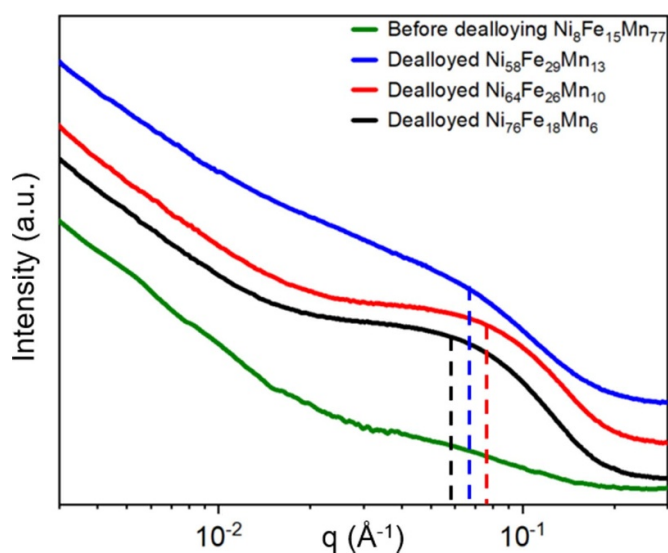| As-printed nominal composition	Condition	Method	Ni (at. %)	Fe (at. %)	Mn (at. %)
$Ni_{14}Fe_{18}Mn_{68}$	Sintered	EDS	15	19	66
		ICP	10.0	21.9	68.1
	Dealloyed	EDS	58	29	13
		ICP	62.6	24.6	12.8
$Ni_{12}Fe_{15}Mn_{73}$	Sintered	EDS	9	17	74
		ICP	8.4	18.6	73.0
	Dealloyed	EDS	64	26	10
		ICP	63.0	27.5	9.5
$Ni_9Fe_{11}Mn_{80}$	Sintered	EDS	8	15	77
		ICP	8.6	11.9	79.5
	Dealloyed	EDS	76	18	6
		ICP	76.3	18.5	5.2

Figure 5. SAXS patterns of the NiFeMn samples before and after dealloying. $Ni_8Fe_{15}Mn_{77}$ alloy was used to represent the NiFeMn ternary MPEAs before dealloying. The other two ternary MPEAs show similar patterns and are not shown here. The profile for the sample before dealloying shows a straight line, while the dealloyed samples for the three considered NiFeMn ternary MPEAs all show a peak near a q-value of 0.075 Å^{-1}, 0.065 Å^{-1}, 0.055 Å^{-1} for $Ni_{64}Fe_{26}Mn_{10}$ (red curve), $Ni_{58}Fe_{29}Mn_{13}$ (blue curve), and $Ni_{76}Fe_{18}Mn_6$ (black curve), respectively.

3.3. Case study: compositional effect on electrocatalytic OER performance

To illustrate the feasibility of our integrated approach to tune the composition of MPEAs and how this can be applied in high-throughput material discovery, here we show a case study on the compositional effect of hierarchically porous NiFeMn MPEAs towards electrocatalytic OER performance. Figure 7(a) shows the CV curves of the three dealloyed NiFeMN MPEA catalysts. Despite the compositional variance, they share a similar feature by exhibiting a pair of redox peaks between 1.35–1.55 V vs. RHE, followed by a positive

oxidation current at higher potentials. The redox peaks are known to be a conversion between Ni^{2+} and Ni^{3+} with the following reaction [44, 71]:

$$Ni(OH)_2 + OH^- \leftrightarrow NiOOH + H_2O + e^- \tag{2}$$

Due to the higher Ni content, the peak current of dealloyed $Ni_{76}Fe_{18}Mn_6$ MPEA is higher than the other two NiFeMn MPEA catalysts. The positive current beyond 1.55 V vs. RHE corresponds to OER on NiOOH surfaces. Previous studies have shown that a Ni:Fe ratio of 2:1 exhibits the optimal OER performance [44]. As shown in figure 7(a) inset, the overpotential required to achieve a current of 0.5 A g^{-1} for OER (thus subtracting the current contribution from Ni^{2+} oxidation) increases in the order of $Ni_{58}Fe_{29}Mn_{13} \leqslant Ni_{64}Fe_{26}Mn_{10} < Ni_{76}Fe_{18}Mn_6$, with $Ni_{58}Fe_{29}Mn_{13}$ exhibiting an overpotential of ∼330 mV which is similar to or lower than many catalysts that utilize the costly IrO$_x$-based electrodes [72]. Our results suggest that the OER performance improves as the composition approaches a Ni:Fe ratio of 2:1, which is consistent with the results from the literature [44]. The intrinsic activity of electrocatalysts, irrespective of their thickness and mass loading, can be further examined by their Tafel slopes [73]. Figure 7(b) shows that at the initial stage of OER, the $Ni_{58}Fe_{29}Mn_{13}$ and $Ni_{64}Fe_{26}Mn_{10}$ MPEAs exhibit a similar Tafel slope of ∼90 mV dec^{-1}, which is much lower than $Ni_{76}Fe_{18}Mn_6$ (∼150 mV dec^{-1}). We speculate that the similar Tafel slopes for $Ni_{58}Fe_{29}Mn_{13}$ and $Ni_{64}Fe_{26}Mn_{10}$ arise from their similar bulk compositions ($Ni_{62.6}Fe_{24.6}Mn_{12.8}$ vs. $Ni_{63.0}Fe_{27.5}Mn_{9.5}$ measured by ICP as shown in table 1). The higher Tafel slope value for $Ni_{76}Fe_{18}Mn_6$ also confirms its inferior intrinsic activity as it has a composition furthest from the optimal ratio, in accordance with the CV results in figure 7(a).

Finally, we investigated the stability of the electrocatalyst, an essential aspect in evaluating OER since many catalysts suffer from performance degradation over time due to catalyst surface reconstruction, lattice oxygen evolution, dissolution,
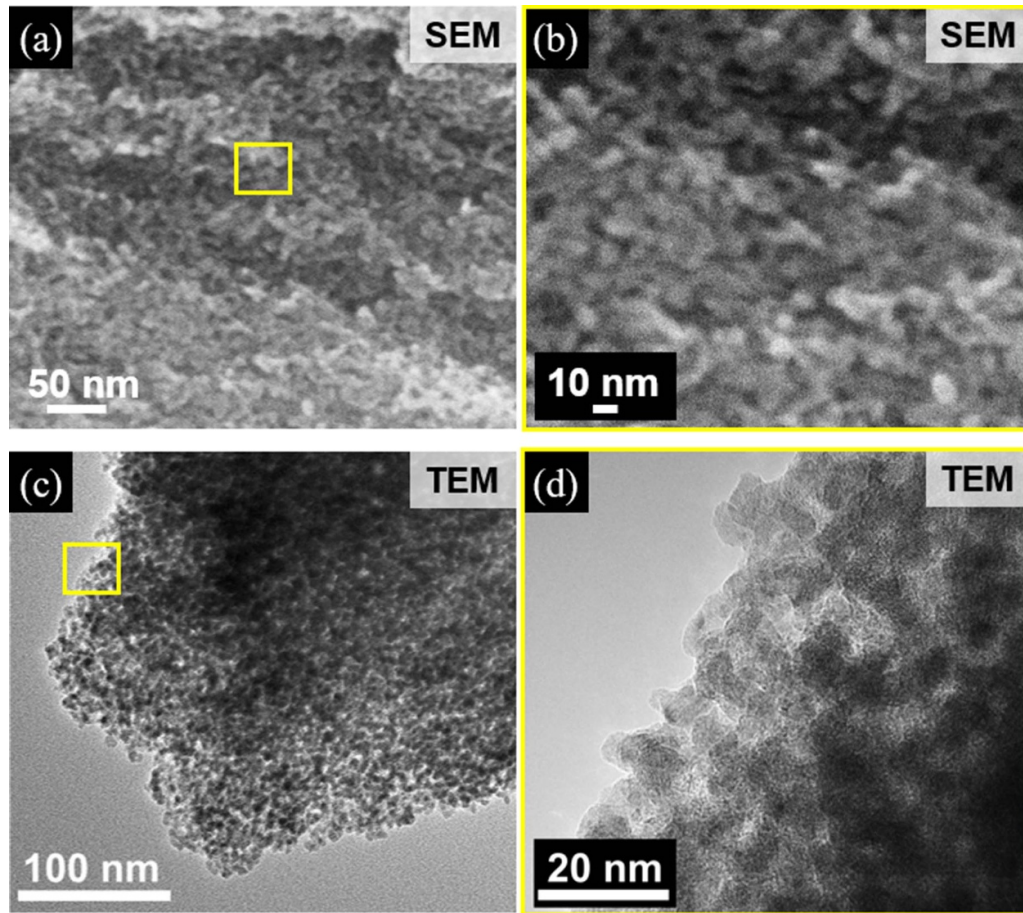
Figure 6. Typical morphology of dealloyed NiFeMn MPEA in the case of $Ni_{76}Fe_{18}Mn_6$. (a) and (c) are low-magnification SEM and TEM images, respectively. (b) and (d) are respective high-magnification SEM and TEM images of highlighted yellow regions in (a) and (c).
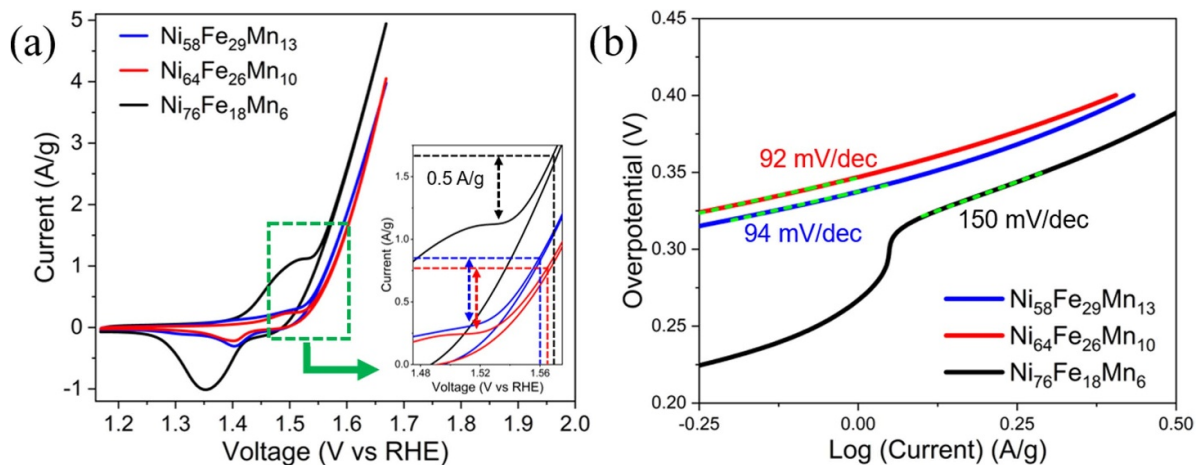

Figure 7. (a) CV tests of NiFeMn MPEA electrocatalysts with different compositions in 1M NaOH at 1 mV s^{-1}. Inset shows the overpotential to achieve 0.5 A g^{-1} OER activity increases in the order of $Ni_{58}Fe_{29}Mn_{13}$ (blue) $\leqslant$ $Ni_{64}Fe_{26}Mn_{10}$ (red) $<$ $Ni_{76}Fe_{18}Mn_6$ (black). (b) Tafel plots derived from CV curves in (a). Tafel slope increases in the order of $Ni_{58}Fe_{29}Mn_{13}$ (blue) $\approx$ $Ni_{64}Fe_{26}Mn_{10}$ (red) $<$ $Ni_{76}Fe_{18}Mn_6$ (black), suggesting the higher intrinsic catalytic activity as Ni:Fe ratio approaches an optimal value of 2:1.

among others [74]. Figure 8 shows the stability test of the representative $Ni_{64}Fe_{26}Mn_{10}$ MPEA catalyst in 1 M NaOH solution under moderate (25 mA cm^{-2}) and high (100 mA cm^{-2}) current densities: under 25 mA cm^{-2}, a stable overpotential of 500 mV was recorded for 20 h, while under 100 mA cm^{-2},

the overpotential started from 900 mV and dropped down to 850 mV after 20 h. Despite the relatively large overpotential, the electrocatalyst did not show a sign of degradation after 20 h when the experiment was intentionally stopped, suggesting its stable performance towards OER applications.
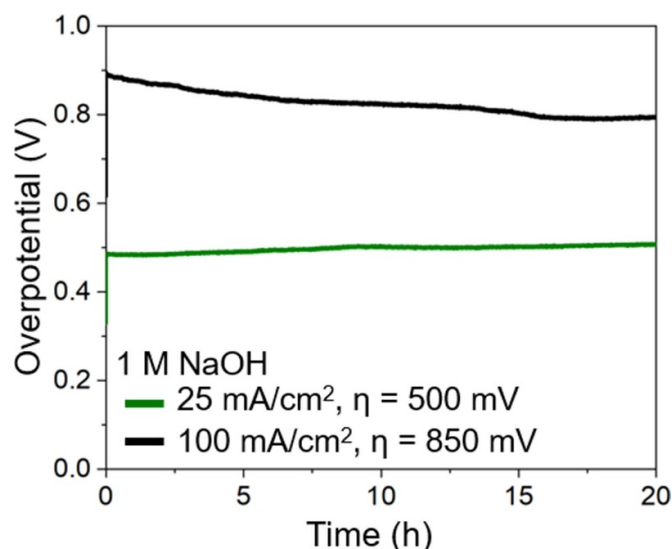
Figure 8. OER stability test of a representative NiFeMn ($Ni_{64}Fe_{26}Mn_{10}$) MPEA catalyst in 1 M NaOH solution. The electrocatalyst achieves a current density of 25 mA cm^{-2} and 100 mA cm^{-2} over 20 h at an overpotential of 500 mV (green) and 850 mV (black), respectively.

4. Conclusions

In summary, this work provides a new pathway to accelerate both the discovery and the production of novel multiscale MPEAs. The integrated processing framework of DIW-based additive manufacturing, followed by thermal sintering and chemical dealloying, is used to produce hierarchically porous NiFeMn MPEAs using pure elemental particles as the starting raw materials. The use of elemental particles allows a flexible control of the MPEA compositions to be synthesized and tested simultaneously by simply adjusting the stoichiometric ratios of the constituent particles in the ink. This versatility allows accelerated exploration of the vast compositional space of MPEAs, as exemplified in this work by the considered three representative compositions. In addition, the methodology outlined in this work offers a means to rapidly and efficiently prepare large quantities of dealloyed nanoporous materials due to the hierarchical nature of the 3D-printed and sintered architectures. The macro- and meso-scale printed channels allow the dealloying corroding medium to spread throughout the printed structure. The microscale pores and filaments after controlled sintering enable the diffusion length (i.e. distance corroding medium must traverse to complete the dealloying process) to remain small even as the sample size and mass are large. Such a process stands in contrast to the typical dealloying of thin films or ribbons, where the entire sample thickness must remain on the order of microns to ensure reasonable dealloying times. Composition-dependent OER performance was investigated as a case study, while we hope this technique can be extended beyond OER to many other compositionally complex alloy systems for electrochemical reactions as well as high-throughput material discovery. For instance, future studies will also explore

multicomponent metal catalysts for hydrogen evolution reactions and oxygen reduction reactions towards a myriad of renewable energy applications.

5. Future perspectives

The design principle of an (electro)catalyst, especially when gas-phase reactants/products are involved such as OER, ORR, and HER, mainly follows two key factors: the intrinsic activity of the catalyst, and the mass transport kinetics of the architecture. In the former case, MPEAs with earth-abundant elements have emerged as a promising alternative to novel metals based on Au, Pt, Pd, etc. In the latter case, nanostructured materials with multi-level porosity provide improved molecular diffusion as well as high surface area. Nevertheless, these two categories are rarely linked, and methodologies to develop multiscale MPEA (electro)catalysts are not well-established. This study combines DIW additive manufacturing with chemical dealloying to provide a facile synthesis approach towards multiscale NiFeMn MPEAs with porosity ranging from 10 nm scale to 100 μm scale. Furthermore, as evidenced from the OER case study, the tailored composition of the NiFeMn MPEAs has impact on the catalytic activity.

Moving forward, we anticipate that this integrated approach, when combined with machine-learning-based simulation, can be utilized for exploring the vast compositional space of MPEAs. This is of great importance since the composition-performance relationship is often non-linear, complicated by the underlying phases and microstructures of the MPEAs, thus necessitates a comprehensive and high-throughput materials discovery.

Conflict of interest

There are no conflicts to declare.

Authors's contribution

Shahryar Mooraj: Investigation, Conceptualization, Formal analysis, Writing—original, Writing—review & editing, Methodology, Visualization. Jintao Fu: Investigation, Conceptualization, Formal analysis, Writing—review & editing, Methodology. Shuai Feng: Investigation, Formal analysis, Writing—review & editing. Alexander K. Ng: Investigation, Formal analysis, Writing—review & editing. Eric B. Duoss: Supervision, Writing—review & editing. Sarah E. Baker: Supervision, Writing—review & editing. Cheng Zhu: Supervision, Conceptualization, Writing—review & editing. Eric Detsi: Supervision, Conceptualization, Funding acquisition, Writing—review & editing. Wen Chen: Supervision, Conceptualization, Funding acquisition, Writing—original, Writing—review & editing, Conceptualization.

ORCID iD

Wen Chen ⬛ https://orcid.org/0000-0003-2048-1107

References

[1] Chen Y, Xie B, Liu B, Cao Y, Li J, Fang Q and Liaw P K A 2022 Focused review on engineering application of multi-principal element alloy *Front. Mater.* **8** 816309

[2] Patel K, Mahajan C, Muskeri S and Mukherjee S 2023 Corrosion behavior of refractory high-entropy alloys in FLiNaK molten salts *Metals* **13** 450

[3] Zhang J Y *et al* 2022 Recent development of chemically complex metallic glasses: from accelerated compositional design, additive manufacturing to novel applications *Mater. Futures* **1** 012001

[4] Zhang L, Huang R, Zhou F, Amar A, Yan H, Zhang Y and Lu Y 2024 Remarkable improved strength and ductility in brittle eutectic high-entropy alloy via a novel spheroidization and recrystallization strategy *J. Mater. Sci. Technol.* **187** 177–87

[5] Moon J, Tabachnikova E, Shumilin S, Hryhorova T, Estrin Y, Brechtl J, Liaw P K, Wang W, Dahmen K A and Kim H S 2021 Unraveling the discontinuous plastic flow of a Co-Cr-Fe-Ni-Mo multiprincipal-element alloy at deep cryogenic temperatures *Phys. Rev. Mater.* **5** 083601

[6] Shams S A A, Bae J W, Kim J N, Kim H S, Lee T and Lee C S 2022 Origin of superior low-cycle fatigue resistance of an interstitial metastable high-entropy alloy *J. Mater. Sci. Technol.* **115** 115–28

[7] Dai W, Lu T and Pan Y 2019 Novel and promising electrocatalyst for oxygen evolution reaction based on MnFeCoNi high entropy alloy *J. Power Sources* **430** 104–11

[8] Tang J, Xu J L, Ye Z G, Li X B and Luo J M 2021 Microwave sintered porous CoCrFeNiMo high entropy alloy as an efficient electrocatalyst for alkaline oxygen evolution reaction *J. Mater. Sci. Technol.* **79** 171–7

[9] Siow J H, Bilad M R, Caesarendra W, Leam J J, Bustam M A, Sambudi N S, Wibisono Y and Mahlia T M I 2021 Progress in development of nanostructured manganese oxide as

catalyst for oxygen reduction and evolution reaction *Energies* **14** 6385

[10] Ren J *et al* 2022 Strong yet ductile nanolamellar high-entropy alloys by additive manufacturing *Nature* **608** 62–68

[11] George E P, Curtin W A and Tasan C C 2020 High entropy alloys: a focused review of mechanical properties and deformation mechanisms *Acta Mater.* **188** 435–74

[12] Ter-Isahakyan A, Rau J S and Balk T J 2022 High entropy alloys with hexagonal close-packed structure derived from thin film combinatorial approach *J. Alloys Compd.* **893** 162293

[13] Li W, Xie D, Li D, Zhang Y, Gao Y and Liaw P K 2021 Mechanical behavior of high-entropy alloys *Prog. Mater. Sci.* **118** 100777

[14] Yan X, Zou Y and Zhang Y 2022 Properties and processing technologies of high-entropy alloys *Mater. Futures* **1** 022002

[15] Toda-Caraballo I and Rivera-Díaz-del-Castillo P E J 2015 Modelling solid solution hardening in high entropy alloys *Acta Mater.* **85** 14–23

[16] Santodonato L J, Zhang Y, Feygenson M, Parish C M, Gao M C, Weber R J K, Neuefeind J C, Tang Z and Liaw P K 2015 Deviation from high-entropy configurations in the atomic distributions of a multi-principal-element alloy *Nat. Commun.* **6** 5964

[17] Wang X, Guo W and Fu Y 2021 High-entropy alloys: emerging materials for advanced functional applications *J. Mater. Chem.* A **9** 663–701

[18] Liu L-H, Li N, Han M, Han J-R and Liang H-Y 2022 Scalable synthesis of nanoporous high entropy alloys for electrocatalytic oxygen evolution *Rare Met.* **41** 125–31

[19] You J, Yao R, Ji W, Zhao Y and Wang Z 2022 Research of high entropy alloys as electrocatalyst for oxygen evolution reaction *J. Alloys Compd.* **908** 164669

[20] Chen Y *et al* 2019 Effective promotion of oxygen reduction reaction by in situ formation of nanostructured catalyst *ACS Catal.* **9** 7137–42

[21] Liu X, Jia H, Sun Z, Chen H, Xu P and Du P 2014 Nanostructured copper oxide electrodeposited from copper(II) complexes as an active catalyst for electrocatalytic oxygen evolution reaction *Electrochem. Commun.* **46** 1–4

[22] Qiu H-J, Fang G, Wen Y, Liu P, Xie G, Liu X and Sun S 2019 Nanoporous high-entropy alloys for highly stable and efficient catalysts *J. Mater. Chem.* A **7** 6499–506

[23] Li W *et al* 2022 Scalable and selective deuteration of (hetero)arenes *Nat. Chem.* **14** 334–41

[24] Goulas A and van Ommen J R 2014 Scalable production of nanostructured particles using atomic layer deposition *KONA* **31** 234–46

[25] Leng J, Wang Z, Wang J, Wu H-H, Yan G, Li X, Guo H, Liu Y, Zhang Q and Guo Z 2019 Advances in nanostructures fabricated *via* spray pyrolysis and their applications in energy storage and conversion *Chem. Soc. Rev.* **48** 3015–72

[26] Fu J, Welborn S S and Detsi E 2022 Dealloyed air- and water-sensitive nanoporous metals and metalloids for emerging energy applications *ACS Appl. Energy Mater.* **5** 6516–44

[27] Gong T, Rudman K K, Guo B and Hall A S 2023 Electrochemical synthesis of nanostructured ordered intermetallic materials under ambient conditions *Acc. Chem. Res.* **56** 1373–83

[28] Matharu Z, Daggumati P, Wang L, Dorofeeva T S, Li Z and Seker E 2017 Nanoporous-gold-based electrode morphology libraries for investigating structure–property relationships in nucleic acid based electrochemical biosensors *ACS Appl. Mater. Interfaces* **9** 12959–66

[29] Gan L, Heggen M, O'Malley R, Theobald B and Strasser P 2013 Understanding and controlling nanoporosity

formation for improving the stability of bimetallic fuel cell catalysts *Nano Lett.* **13** 1131–8

[30] McCue I, Benn E, Gaskey B and Erlebacher J 2016 Dealloying and dealloyed materials *Annu. Rev. Mater. Res.* **46** 263–86

[31] Rittiruam M, Noppakhun J, Setasuban S, Aumnongpho N, Sriwattana A, Boonchuay S, Saelee T, Wangphon C, Ektarawong A and Chammingkwan P 2022 High-throughput materials screening algorithm based on first-principles density functional theory and artificial neural network for high-entropy alloys *Sci. Rep.* **12** 16653

[32] Gregoire J M, Van Campen D G, Miller C E, Jones R J R, Suram S K and Mehta A 2014 High-throughput synchrotron x-ray diffraction for combinatorial phase mapping *J. Synchrotron Radiat.* **21** 1262–8

[33] Al Hasan N M, Hou H, Sarkar S, Thienhaus S, Mehta A, Ludwig A and Takeuchi I 2020 Combinatorial synthesis and high-throughput characterization of microstructure and phase transformation in Ni–Ti–Cu–V quaternary thin-film library *Engineering* **6** 637–43

[34] Melia M A, Whetten S R, Puckett R, Jones M, Heiden M J, Argibay N and Kustas A B 2020 High-throughput additive manufacturing and characterization of refractory high entropy alloys *Appl. Mater. Today* **19** 100560

[35] Banko L, Krysiak O A, Pedersen J K, Xiao B, Savan A, Löffler T, Baha S, Rossmeisl J, Schuhmann W and Ludwig A 2022 Unravelling composition–activity–stability trends in high entropy alloy electrocatalysts by using a data-guided combinatorial synthesis strategy and computational modeling *Adv. Energy Mater.* **12** 2103312

[36] Roy D, Mandal S C and Pathak B 2022 Machine learning assisted exploration of high entropy alloy-based catalysts for selective CO_2 reduction to methanol *J. Phys. Chem. Lett.* **13** 5991–6002

[37] Yeh J-W 2013 Alloy design strategies and future trends in high-entropy alloys *JOM* **65** 1759–71

[38] Liang A, Goodelman D C, Hodge A M, Farkas D and Branicio P S 2023 CoFeNiTi and CrFeNiTi high entropy alloy thin films microstructure formation *Acta Mater.* **257** 119163

[39] Alberi K *et al* 2019 The 2019 materials by design roadmap *J. Phys. D: Appl. Phys.* **52** 013001

[40] Sharma L, Katiyar N K, Parui A, Das R, Kumar R, Tiwary C S, Singh A K, Halder A and Biswas K 2022 Low-cost high entropy alloy (HEA) for high-efficiency oxygen evolution reaction (OER) *Nano Res.* **15** 4799–806

[41] Qiu H-J, Fang G, Gao J, Wen Y, Lv J, Li H, Xie G, Liu X and Sun S 2019 Noble metal-free nanoporous high-entropy alloys as highly efficient electrocatalysts for oxygen evolution reaction *ACS Mater. Lett.* **1** 526–33

[42] Kondapalli V, He X, Khosravifar M, Khodabakhsh S, Collins B, Yarmolenko S, Paz Y Puente A and Shanov V 2021 CVD synthesis of 3D-Shaped 3D graphene using a 3D-Printed Nickel–PLGA catalyst precursor *ACS Omega* **6** 29009–21

[43] Estelle K T and Gozen B A 2022 Complex ink flow mechanisms in micro-direct-ink-writing and their implications on flow rate control *Addit. Manuf.* **59** 103183

[44] Detsi E, Cook J B, Lesel B K, Turner C L, Liang Y-L, Robbennolt S and Tolbert S H 2016 Mesoporous $Ni_{60}Fe_{30}Mn_{10}$ -alloy based metal/metal oxide composite thick films as highly active and robust oxygen evolution catalysts *Energy Environ. Sci.* **9** 540–9

[45] Zhu C, Pascall A J, Dudukovic N, Worsley M A, Kuntz J D, Duoss E B and Spadaccini C M 2019 Colloidal materials for 3*D* printing *Annu. Rev. Chem. Biomol. Eng.* **10** 17–42

[46] Mooraj S, Welborn S S, Jiang S, Peng S, Fu J, Baker S, Duoss E B, Zhu C, Detsi E and Chen W 2020 Three-dimensional hierarchical nanoporous copper via direct ink writing and dealloying *Scr. Mater.* **177** 146–50

[47] Zhu C *et al* 2018 Toward digitally controlled catalyst architectures: hierarchical nanoporous gold via 3D printing *Sci. Adv.* **4** eaas9459

[48] Yokota M, Harada R and Mitani H 1980 Interdiffusion in γ solid solution of the Ni-Mn binary alloy system *Trans. JIM* **21** 409–16

[49] Hegde O, Kulitckii V, Schneider A, Soisson F, Hickel T, Neugebauer J, Wilde G, Divinski S and Fu C-C 2021 Impact of magnetic transition on Mn diffusion in α -iron: correlative state-of-the-art theoretical and experimental study *Phys. Rev.* B **104** 184107

[50] Million B, Růžičková J, Velíšek J and Vřešťál J 1981 Diffusion processes in the Fe-Ni system *Mater. Sci. Eng.* **50** 43–52

[51] Welborn S S and Detsi E 2020 Small-angle x-ray scattering of nanoporous materials *Nanoscale Horiz.* **5** 12–24

[52] Ng A K, Welborn S S and Detsi E 2022 Time-dependent power law function for the post-dealloying chemical coarsening of nanoporous gold derived using small-angle x-ray scattering *Scr. Mater.* **206** 114215

[53] Fu J, Corsi J S, Welborn S S, Basile V, Wang L, Ng A K and Detsi E 2021 Eco-friendly synthesis of nanoporous magnesium by air-free electrolytic dealloying with recovery of sacrificial elements for energy conversion and storage applications *ACS Sustain. Chem. Eng.* **9** 2762–9

[54] Moon Y W, Choi I J, Koh Y H and Kim H E 2015 Macroporous alumina scaffolds consisting of highly microporous hollow filaments using three-dimensional ceramic/camphene-based co-extrusion *J. Eur. Ceram. Soc.* **35** 4623–7

[55] Zhang Y, Sun X, Nomura N and Fujita T 2019 Hierarchical nanoporous copper architectures via 3D printing technique for highly efficient catalysts *Small* **1805432** 1–7

[56] Wang N, Pan Y and Wu S 2018 Relationship between dealloying conditions and coarsening behaviors of nanoporous copper fabricated by dealloying Cu-Ce metallic glasses *J. Mater. Sci. Technol.* **34** 1162–71

[57] Chen Q and Sieradzki K 2013 Mechanisms and morphology evolution in dealloying *J. Electrochem. Soc.* **160** C226–C231

[58] Qiu H-J, Peng L, Li X, Xu H T and Wang Y 2015 Using corrosion to fabricate various nanoporous metal structures *Corros. Sci.* **92** 16–31

[59] Chen L-Y, Yu J-S, Fujita T and Chen M-W 2009 Nanoporous copper with tunable nanoporosity for SERS applications *Adv. Funct. Mater.* **19** 1221–6

[60] Xu C, Li Y, Tian F and Ding Y 2010 Dealloying to nanoporous silver and its implementation as a template material for construction of nanotubular mesoporous bimetallic nanostructures *Chem. Eur. J. Chem. Phys.* **11** 3320–8

[61] Erlebacher J and Seshadri R 2009 Hard materials with tunable porosity *MRS Bull.* **34** 561–8

[62] Jiang Z, Zhang J, Wang K, Chen T, Zhao J, Wang K and Hu J A 2022 novel dealloying strategy for fabricating nanoporous Ag via ζ′-AgGa alloy *Nanotechnology* **33** 195601

[63] Wittstock A , Biener J , Erlebacher J and Bäumer M 2012 *Nanoporous Gold: From an Ancient Technology to a High-Tech Material* (Royal Society of Chemistry) (https://doi.org/10.1039/9781849735285)

[64] Balogh Z and Schmitz G 2014 Diffusion in metals and alloys *Physical Metallurgy* (Elsevier) ch 5, pp 387–559

[65] Mehta A and Sohn Y 2021 Investigation of sluggish diffusion in FCC $Al_{0.25}$CoCrFeNi high-entropy alloy *Mater. Res. Lett.* **9** 239–46

[66] Stepanov N D, Shaysultanov D G, Ozerov M S, Zherebtsov S V and Salishchev G A 2016 Second phase

formation in the CoCrFeNiMn high entropy alloy after recrystallization annealing *Mater. Lett.* **185** 1–4

[67] Zhang L, Du Y, Xu H, Liu S, Liu Y, Zheng F, Dupin N, Zhou H and Tang C 2009 Phase equilibria and thermal analysis in the Fe–Mn–Ni system *Int. J. Mater. Res.* **100** 160–75

[68] Graf M, Ngô B-N D, Weissmüller J and Markmann J 2017 x-ray studies of nanoporous gold: powder diffraction by large crystals with small holes *Phys. Rev. Mater.* **1** 076003

[69] Boldon L, Laliberte F and Liu L 2015 Review of the fundamental theories behind small angle x-ray scattering, molecular dynamics simulations, and relevant integrated application *Nano Rev.* **6** 25661

[70] Welborn S S and Detsi E 2019 Small-angle x-ray scattering of nanoporous materials *Nanoscale Horiz.* **5** 12–24

[71] Qiu Y, Xin L and Li W 2014 Electrocatalytic oxygen evolution over supported small amorphous Ni–Fe nanoparticles in alkaline electrolyte *Langmuir* **30** 7893–901

[72] Shi Z, Wang X, Ge J, Liu C and Xing W 2020 Fundamental understanding of the acidic oxygen evolution reaction: mechanism study and state-of-the-art catalysts *Nanoscale* **12** 13249–75

[73] Surendranath Y, Kanan M W and Nocera D G 2010 Mechanistic studies of the oxygen evolution reaction by a cobalt-phosphate catalyst at neutral pH *J. Am. Chem. Soc.* **132** 16501–9

[74] Chen F-Y, Wu Z-Y, Adler Z and Wang H 2021 Stability challenges of electrocatalytic oxygen evolution reaction: from mechanistic understanding to reactor design *Joule* **5** 1704–31